

Persistent spin helix in Rashba-Dresselhaus ferroelectric CsBiNb₂O₇

Carmine Autieri^{1,2}, Paolo Barone², Jagoda Sławińska³, and Silvia Picozzi²

¹*International Research Centre MagTop, Institute of Physics,*

Polish Academy of Sciences, Aleja Lotników 32/46, PL-02668 Warsaw, Poland

²*Consiglio Nazionale delle Ricerche, Istituto Superconduttori,*

Materiali Innovativi e Dispositivi (CNR-SPIN), c/o Università G. D'Annunzio, I-66100 Chieti, Italy and

³*Department of Physics, University of North Texas, Denton, TX 76203, USA*

(Dated: July 29, 2019)

Ferroelectric Rashba semiconductors (FERSC) are a novel class of multifunctional materials showing a giant Rashba spin splitting which can be reversed by switching the electric polarization. Although they are excellent candidates as channels in spin field effect transistors, the experimental research has been limited so far to semiconducting GeTe, in which ferroelectric switching is often prevented by heavy doping and/or large leakage currents. Here, we report that CsBiNb₂O₇, a layered perovskite of Dion-Jacobson type, is a robust ferroelectric with sufficiently strong spin-orbit coupling and spin texture reversible by electric field. Moreover, we reveal that its topmost valence band's spin texture is quasi-independent from the momentum, as a result of the low symmetry of its ferroelectric phase. The peculiar spin polarization pattern in the momentum space may yield the so-called "persistent spin helix", a specific spin-wave mode which protects the spin from decoherence in diffusive transport regime, potentially ensuring a very long spin lifetime in this material.

PACS numbers: 71.15.am, 73.22.Pr, 63.22.Rc, 68.65.Ac

I. INTRODUCTION

Novel materials with tunable spin properties hold promise to realize logic spintronics devices similar to spin field-effect transistors (spin-FET) proposed by Das and Datta.¹ Recently discovered ferroelectric Rashba semiconductors (FERSC) emerge as excellent candidates for spin-FET channels, because of their unique coupling between spin and polar degrees of freedom enabling a purely electric non-volatile control of the electron's spin.²⁻⁴ The Rashba spin splitting, due to inversion symmetry breaking with a single polar axis in these bulk crystals, can be controlled and permanently reversed by switching the sign of electric polarization, as theoretically predicted and experimentally confirmed in the FERSC prototype material GeTe.⁵ Moreover, being a bulk property, the Rashba spin texture in FERSC has been shown to be hardly affected when interfaced with ferromagnets,^{6,7} which could be important when looking for robustness against the device configuration.

Unveiling peculiar properties of GeTe has stimulated several theoretical studies aiming at the discovery of novel FERSC. Several candidates have been proposed, ranging from similar chalcogenides (SnTe)⁸ to metal-organic halide perovskites, such as (FA)SnI₃,⁹ hexagonal semiconductors (LiZnSb),¹⁰ and oxides (HfO₂, BiAlO₃, SrBiO₃).¹¹⁻¹³ Most of them are robust ferroelectrics with sufficiently large band gaps preventing leakage currents and related problems with ferroelectric switching.¹⁴ These properties, together with large spin-orbit coupling (SOC), constitute essential requirements for realization of FERSC-based devices. On the other hand, strong SOC causes decoherence of electron spins in non-ballistic transport regime, making spin lifetimes of most FERSC too short for practical purposes.

Recent study on two-dimensional ferroelectric materials with in-plane electric polarization and out-of-plane spin polarization induced by SOC suggests that the problem of spin dephasing could be eliminated.¹⁵ In these materials, the symmetries of the crystal enforce the spin texture to be independent from the electron's momentum. Such spin configuration, called persistent spin texture (PST), was first proposed by Schliemann *et al.*¹⁶ for quantum wires with Dresselhaus and Rashba coefficients fine-tuned to have equal strengths. The corresponding spin wave mode emerging in the crystal, known as persistent spin helix (PSH),¹⁷ protects the spins of electrons from dephasing, as they all precess at the same rate and in the same direction after scattering events. The concept of PSH has been recently extended to specific 3D bulk materials where the bulk crystal symmetries, rather than fine tuning of the SOC parameters, can substantially increase the spin lifetime.¹⁸ Interestingly, a unidirectional spin-orbit field necessary to realize a PSH, has been recently predicted in a layered Aurivillius ferroelectric oxide, Bi₂WO₆, where it results from the combination of in-plane polarization and layering-related anisotropy of the electronic structure.¹⁹

Here, we reveal that another ferroelectric layered oxide, CsBiNb₂O₇, possesses a peculiar Rashba-Dresselhaus spin texture, thus combining exceptional properties of FERSC with potentially long spin lifetime of carriers. CsBiNb₂O₇ is a layered perovskite of Dion-Jacobson type with a wide band gap, large ferroelectric polarization and SOC-derived spin splitting of the valence band of the order of 10 meV, which makes it a good FERSC candidate. Our density functional theory (DFT) calculations complemented by $\mathbf{k} \cdot \mathbf{p}$ analysis have shown that the spin texture of the topmost valence band in the ferroelectric phase is close to the persistent spin-helix regime in large areas of the Brillouin zone. The model analysis suggests

that in the ground state a small spin-momentum linear coupling term competes with third order coupling term, yielding a non-trivial spin pattern; on the other hand, for smaller ferroelectric displacements, a conventional Rashba spin texture is restored. Given that the Curie temperature for $\text{CsBiNb}_2\text{O}_7$ is expected to be much far the room temperature, the persistent spin helix emerges as a robust bulk property.

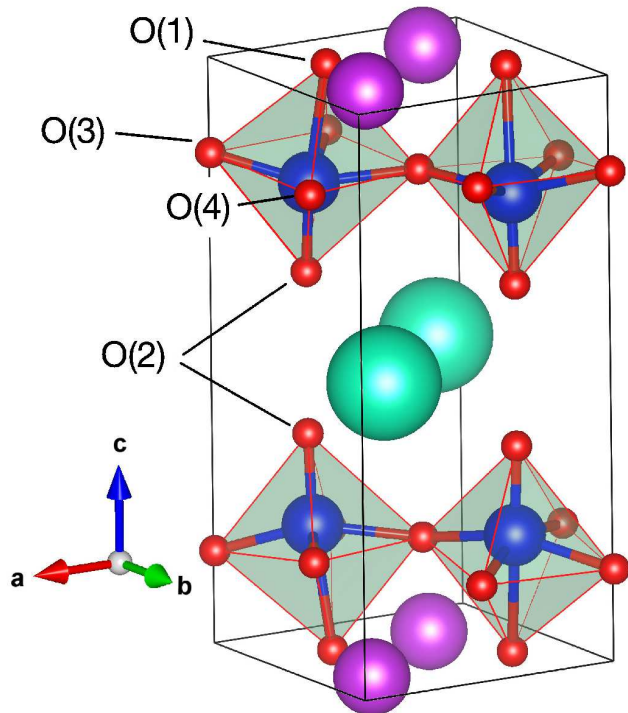


FIG. 1: Crystal structure of the $\text{CsBiNb}_2\text{O}_7$. The NbO_6 octahedra are shown in light green. They are separated along the c -axis by Cs atoms displayed as large green spheres. The Bi atoms in Bi-O planes are marked as violet spheres. O(1)-O(4) denote inequivalent oxygen atoms (small red spheres).

The paper is organized as follows. In Section II, we describe details of the DFT calculations. In Section III A, we discuss the electronic properties and the ferroelectricity of $\text{CsBiNb}_2\text{O}_7$, while Sections III B and III C report the spin textures estimated from DFT and analyzed in the framework of $\mathbf{k} \cdot \mathbf{p}$ theory. Section IV summarizes the conclusions and perspectives of further research.

II. COMPUTATIONAL DETAILS

We have performed first-principles DFT calculations employing the VASP package^{20,21} based on plane wave basis set and projector augmented wave method.^{22,23} We have used a plane-wave energy cut-off of 480 eV and generalized gradient approximation of Perdew-Burke-Ernzerhof as the exchange-correlation functional.²⁴ We have set the experimental internal positions and lattice constants equal to $a=5.49528$ Å, $b=5.42251$ Å and

$c=11.37663$ Å.²⁵ For Brillouin zone integrations, a $8 \times 8 \times 4$ k-points grid has been used. An additional Coulomb repulsion within a DFT+U approach on the Nb atoms has been neglected, because it was estimated to 1-3 eV in 4d perovskite oxides,^{26,27} which is an intermediate value that increases the band gap, but only slightly affects the band structure with empty d -shell. We also note that the effect of the Coulomb repulsion would be even less relevant on the Bi-O states in the valence band as they weakly hybridize with the Nb states. The electric polarization has been calculated using the Berry phase method.²⁸ The spin-orbit coupling (SOC) has been included in all the calculations.

III. RESULTS

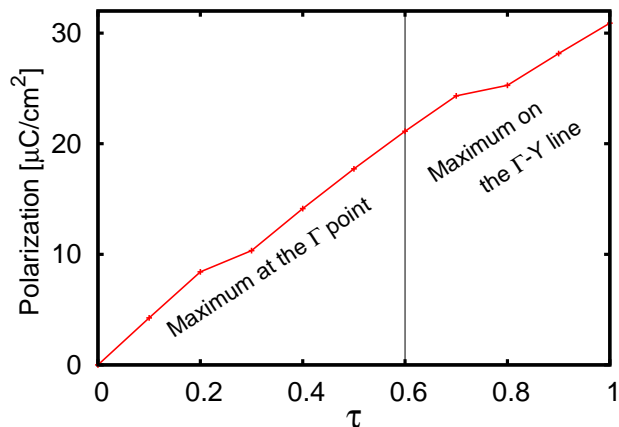


FIG. 2: Total polarization along the ferroelectric path. The vertical line at $\tau = 0.6$ separates two regions with qualitatively different dispersion of the valence band.

A. Electronic properties: band structure and polarization

Figure 1 shows the crystal structure of $\text{CsBiNb}_2\text{O}_7$. Previous studies revealed that it is an $n = 2$ Dion-Jacobson ferroelectric belonging to the space group $P2_1am$ (no. 26) with the in-plane electric polarization parallel to the a axis.²⁹ The contributions of different layers to the ferroelectricity evaluated for this class of materials showed that the origin of polarization is mainly related to the BiO layers.³⁰ Our calculated polarization value of $30.9 \mu\text{C}/\text{cm}^2$ (see Fig. 2) obtained using the experimental atomic positions of $\text{CsBiNb}_2\text{O}_7$ is approximately 20% smaller than the values found in the literature for this and a similar compound $\text{RbBiNb}_2\text{O}_7$,²⁹⁻³¹ which could be attributed to different lattice constants and exchange functionals.

First, we focus on the electronic dispersion within the crystallographic planes orthogonal to the polar axis a ,

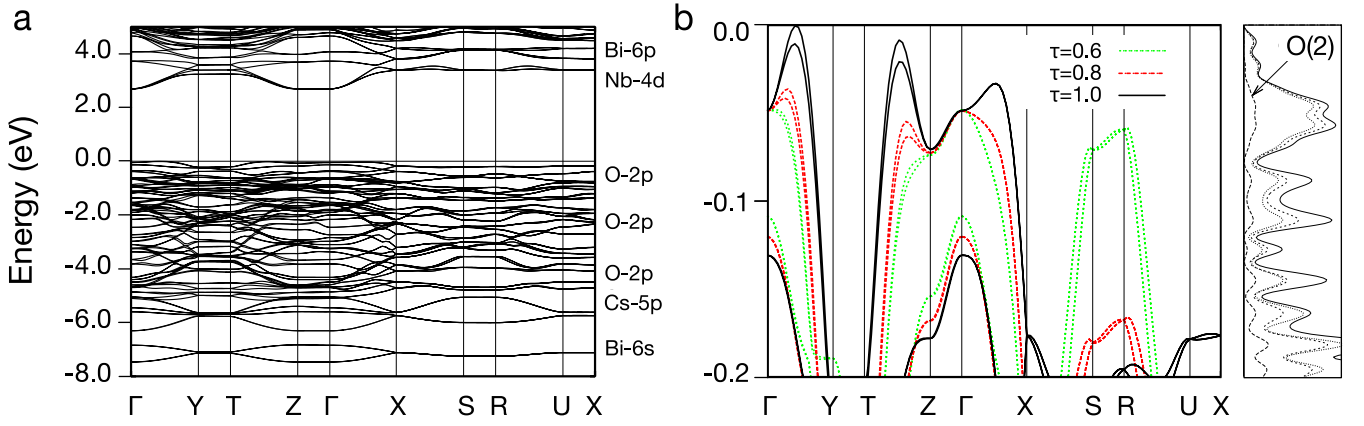


FIG. 3: (a) Band structure of the $\text{CsBiNb}_2\text{O}_7$. The Fermi level is set to zero. (b) Band structure of the topmost valence band calculated for $\tau=0.6$ (dotted green line), 0.8 (dashed red line) and 1.0 (solid black line). The projected DOS of the oxygen atoms is shown as side panel. The solid, dashed, short dashed and dotted black lines represent the DOS of the O(1), O(2), O(3) and O(4) atoms, respectively.

where we expect the largest SOC-derived spin-splitting effects. Nominally, the Nb atoms are in a $4d^0$ configuration while the Cs and Bi atoms are in a $6s^0$ and $6p^0$ configurations, respectively. Finally, all the oxygen atoms are in a $2p^6$ configuration. Figure 3 (a) shows the band structure, plotted along the k -paths lying in two high-symmetry planes orthogonal to the polar axis a . We found a band gap of 2.7 eV, in qualitative agreement with the band structure of $\text{RbBiNb}_2\text{O}_7$,³¹ another compound of the same class. In the polar phase, the band gap is indirect with the minimum of the conduction band at Γ and the maximum of the valence band along the Γ -Y line. We found that the dispersion along the z -axis perpendicular to the layers is reduced by almost an order of magnitude with respect to the in-plane dispersion, similar to other $4d$ layered perovskites.^{32,33}

The orbital composition of the bands is displayed on the right-hand side of Fig. 3(a). We found that between -7.5 eV and -5.5 eV, the electronic structure is mostly of Bi-6s and Cs-5p character, respectively. From -5.5 eV up to the Fermi level, the dispersion is dominated by the oxygen states. We note that there are 4 inequivalent oxygen atoms in the unit cell, as shown in Fig. 1. The O(1) and O(2) atoms are the apical oxygens of the NbO_6 octahedra; they are qualitatively different, since O(1) belongs to the Bi plane and O(2) does not. The O(3) and O(4) atoms are the planar oxygens of the NbO_6 octahedra and they are both first neighbors of the Bi atoms. The density of states just below the Fermi level is contributed by the atoms O(1), O(3) and O(4) strongly hybridizing with Bi states. The contribution from the atoms O(2) is not relevant, as shown in the DOS of Fig. 3(b). Finally, the bottom of the conduction band is composed by Nb-4d bands, while the higher conduction bands display the Bi-6p character.

As a next step, we have investigated in more detail the topmost valence band, which is the most interesting

part of the electronic structure. Figure 3 (b) presents the dispersion energy region closest to the Fermi level (black lines); we can observe a non-negligible spin-splitting close to the Γ point, namely along the lines Γ -Z and Γ -Y corresponding to the direction perpendicular to the polar axis in the reciprocal space. Since the system is layered, the splitting is much larger within the basal plane along the Γ -Y line. The spin-orbit splitting at the maximum of the valence band achieves 10 meV. In addition, we have analyzed the evolution of the valence band versus the ferroelectric displacement, defined as $\tau=0$ for the paraelectric structure and $\tau=1$ for the experimental ferroelectric phase (see Fig. 3(b)). It is clear that the position of the valence band maximum (VBM) strongly depends on the ferroelectric distortion. A decrease in τ reduces the spin-orbit splitting and moves the position of the VBM towards Γ . At the same time, the topmost valence bands in the plane $k_x = \pi/a$ are shifted to lower energies. We have found that the change of behavior occurs at $\tau \sim 0.6$; below this value, the position of the VBM is at the Γ point, while for $\tau > 0.6$ it gets shifted along the Γ -Y line. As a consequence, the gap changes from direct to indirect as a function of the ferroelectric displacement. The Bi- and O-like valence bands are strongly influenced by SOC, while the lowest Nb conduction bands remain almost unaffected.

B. From the Rashba spin texture to the persistent spin helix

We have further investigated the evolution of the energy dispersion and the corresponding spin texture of the topmost valence band as a function of the ferroelectric displacement τ . We have focused on the most interesting area of the Brillouin zone at $k_x=0$. Figure 4(a) shows the valence band for $\tau=0.6$ in the k_y range between $-\frac{\pi}{2b}$

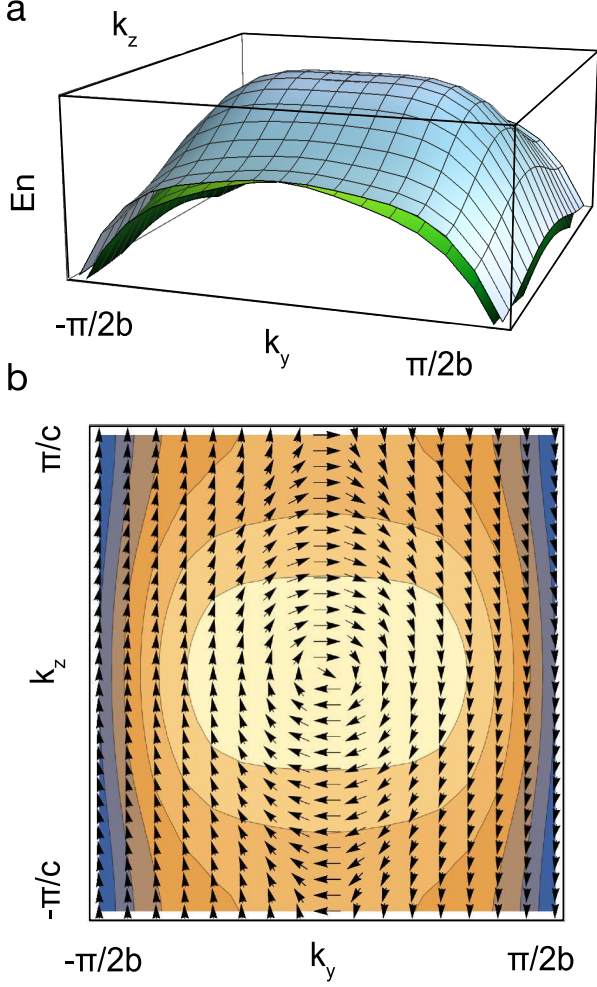


FIG. 4: (a) Spin-split energy bands induced by the spin-momentum coupling at $\tau=0.6$ calculated from first principles. (b) Corresponding spin texture of the valence band at $\tau=0.6$. Arrows denote in-plane spins whereas the color scale shows the energy difference from the Fermi level. The light yellow denotes the regions close to the Fermi level, while dark blue denotes the regions far from the Fermi level.

and $\frac{\pi}{2b}$ and in the k_z range between $-\frac{\pi}{c}$ and $\frac{\pi}{c}$. The dispersion reveals a negative effective mass both along the k_y and k_z axis, as well as a strong dependence on k_y and a weak dependence on k_z (most likely due to the layered structure of $\text{CsBiNb}_2\text{O}_7$). Although this anisotropy is reflected also in the spin texture [cfr Fig. 4(b)], the latter closely resembles the conventional Rashba-like one. As can be observed in Fig. 5(a), at $\tau=1.0$ the dispersion is dramatically different. The effective mass is still negative along the k_z , but it becomes positive along the k_y direction. Even a more striking change can be noticed in the spin texture reported in Fig. 5(b), especially at small momenta around Γ , where we have found a complex pattern of spin polarization, different either from Rashba- and Dresselhaus-like spin textures. The most important feature, however, is the spin fixed along the z -direction

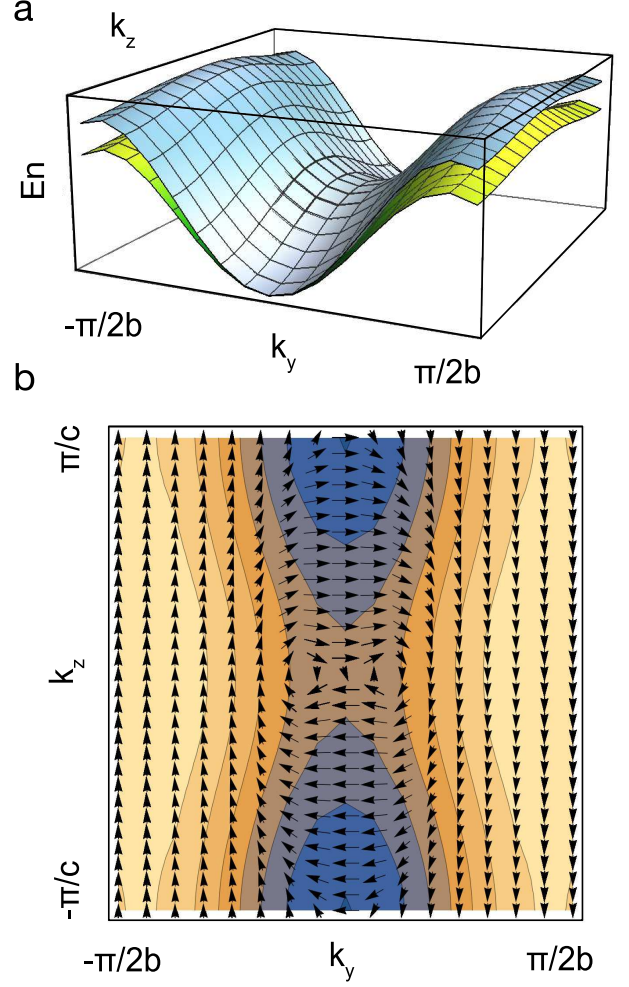


FIG. 5: (a) Spin-split energy bands induced by the spin-momentum coupling for $\tau=1.0$ calculated from first principles. (b) Corresponding spin texture of the valence band at $\tau=1.0$. Arrows denote in-plane spins whereas the color scale shows the energy difference from the Fermi level. The light yellow denotes the regions close to the Fermi level, while dark blue denotes the regions far from the Fermi level.

in a wide region around $k_y \approx \pm \frac{\pi}{2b}$, which gives rise to a persistent spin texture pattern.

Before analyzing in detail the mechanisms driving such spin polarizations, let us briefly compare our results with known 3D crystals in which PST is enforced by the symmetries. For example, in prototype BiInO_3 and recently proposed Bi_2WO_6 , the band splittings are substantially larger, 260 and 70 meV, respectively.^{18,19} This could make them more suitable for room temperature functionalities than $\text{CsBiNb}_2\text{O}_7$ with spin splitting of only 10 meV. However, the new and intriguing property of the latter is the PSH residing in the valence band, which opens a perspective for its direct observation using spin- and angle-resolved photoemission spectroscopy (ARPES) without the need of any additional doping. Furthermore, despite the SOC in $\text{CsBiNb}_2\text{O}_7$ not being perfectly unidi-

rectional over the entire BZ, we note that the previously studied ferroelectric oxides also reveal deviations from the ideal PST. Thus, we are convinced that the pattern shown in Fig. 5(b) can still result in a reduction of spin decoherence in the diffusive transport regime in this material.

C. $\mathbf{k} \cdot \mathbf{p}$ analysis of valence-band spin polarizations

In order to understand the SOC-induced spin-splitting and the non-trivial spin textures of $\text{CsBiNb}_2\text{O}_7$, we derive a minimal $\mathbf{k} \cdot \mathbf{p}$ model for $J = 1/2$ states, enforcing the specific symmetry properties of the system. The point group of the Γ point is C_{2v} , consisting in a two-fold rotations around the polar axis (chosen parallel to x , consistently with the $P2_1am$ setting used in DFT calculations) and two mirror operations about two planes containing the polar axis. We notice that coexisting Rashba and Dresselhaus couplings are generally allowed within this point-group symmetry⁹, which may lead to PSH once Rashba and Dresselhaus coupling constants compensate exactly¹⁶. The calculated electronic structure further suggests that the linear spin-momentum coupling is quite small, the spin-splitting being dominated by the third-order coupling (see, e.g., Fig. 3(b)). The minimal model H_{RD} with Rashba and Dresselhaus couplings up to third-order in momentum, which includes all symmetry-allowed terms, reads as:

$$H_{RD} = E_0 + \alpha(k) k_y \sigma_z + \beta(k) k_z \sigma_y \quad (1)$$

where k_y, k_z are the cartesian components of crystal momentum in the plane perpendicular to the polar axis a and σ are Pauli matrices describing spin degrees of freedom in the same reference system. The free-electron (parabolic) contribution is $E_0 = \hbar^2 k_y^2 / 2m_y^* - \hbar^2 k_z^2 / 2m_z^*$, where we assumed opposite effective masses m_y^*, m_z^* along the orthogonal directions k_y and k_z , consistently with the DFT calculations.

The k -dependent spin-orbit coupling constants in the chosen reference frame are

$$\alpha(k) = \alpha^{(1)} + \alpha^{(3)} k^2 + \gamma_\alpha (k_y^2 - k_z^2) \quad (2)$$

$$\beta(k) = \beta^{(1)} + \beta^{(3)} k^2 + \gamma_\beta (k_y^2 - k_z^2), \quad (3)$$

where $\alpha^{(3)}, \beta^{(3)}$ are k^2 renormalization terms of the linear spin-orbit coupling constants, while $\gamma_\alpha, \gamma_\beta$ account for the k -cubic anisotropic interactions.

The explicit expressions of spin expectation values for model (1) can be easily derived, reading:

$$\begin{aligned} \langle \sigma_y^\pm \rangle &= \pm \frac{\beta(k) k_z}{\sqrt{\alpha(k)^2 k_y^2 + \beta(k)^2 k_z^2}} \\ \langle \sigma_z^\pm \rangle &= \pm \frac{\alpha(k) k_y}{\sqrt{\alpha(k)^2 k_y^2 + \beta(k)^2 k_z^2}}, \end{aligned} \quad (4)$$

which show the dependence of the spin directions onto the sign of the k -dependent coupling constants $\alpha(k), \beta(k)$. The pure linear Rashba (Dresselhaus) limit is recovered when $\alpha^{(1)} = -\beta^{(1)}$ ($+\beta^{(1)}$) and $\alpha^{(3)} = \beta^{(3)} = 0$, while the cubic Dresselhaus term is obtained for $\gamma_\alpha = -\gamma_\beta$. A Rashba-like (Dresselhaus-like) spin texture is also expected when the k -dependent coupling constants $\alpha(k), \beta(k)$ display the same relative signs as above, the spin-polarization pattern being possibly modulated by the anisotropy of the coupling terms. On the other hand, the persistent spin helix would be realized if $\alpha(k)$ or $\beta(k)$ vanishes, leaving a unique spin quantization axis (\hat{y} or \hat{z} , respectively).

Aiming at a quantitative analysis, we fitted the model parameters from the sum and the difference between the two topmost valence bands along the Γ -Y and Γ -Z lines. The effective masses are then obtained by fitting the sum of the two topmost valence bands, while from the difference we get the odd terms $\alpha^{(1)}, \alpha^{(3)} + \gamma_\alpha, \beta^{(1)}$ and $\beta^{(3)} - \gamma_\beta$ related to the spin-orbit parameters. Results are reported in Table I. Unfortunately, we were not able to determine accurately the single values of $\alpha^{(3)}, \beta^{(3)}, \gamma_\alpha$ and γ_β , which would have required to fit the bands away from the high-symmetry Γ -Y and Γ -Z lines, introducing additional numerical uncertainty. Nevertheless, the linear spin-momentum coupling constants are two to three order of magnitude smaller than the cubic ones. On the other hand, assuming for simplicity that $\gamma_\alpha = \gamma_\beta = 0$, the coupling constant $\alpha^{(3)}$ is one order of magnitude larger than $\beta^{(3)}$, explaining the partial compensation of Rashba and Dresselhaus effects and confirming the almost unidirectional spin-orbit field at large momenta along the Γ -Y line. Finally, the opposite signs of the small linear $\alpha^{(1)}$ and cubic $\alpha^{(3)}$ coupling constants can explain the observed non-trivial spin-polarization patterns at small momenta. In fact, as long as $|\alpha^{(1)}| > |\alpha^{(3)} k^2|$ - i.e., very close to the Γ point - the two k -dependent coupling constants $\alpha(k)$ and $\beta(k)$ display the same sign, being both negative, thus supporting a Dresselhaus-like spin-texture; the Rashba-like features emerge again at larger momenta, where the sign of $\alpha(k)$, dominated by the cubic $\alpha^{(3)}$ coupling constant, is opposite to that of $\beta(k)$. As a consequence, the spin-polarization pattern shown in Fig. 6(left panel) is realized, which already agrees qualitatively well with the DFT results shown in Fig. 5(b). We notice that such peculiar spin-texture could not be reproduced by neglecting the k^2 renormalization terms, i.e., for $\alpha^{(3)} = \beta^{(3)} = 0$ and assuming the k -cubic spin splitting as arising solely from the SOC parametrized by $\gamma_\alpha, \gamma_\beta$. In order to get some insight on the role of such k -cubic anisotropic term, and having assessed the primary role of the anisotropy of $\alpha^{(3)}$ and $\beta^{(3)}$, we checked how the spin-polarization pattern is affected by including a cubic Dresselhaus term (parametrized by $\gamma/2 = \gamma_\alpha = -\gamma_\beta$) and assuming $\beta^{(3)} = f\alpha^{(3)}$, where f is an arbitrary independent parameter quantifying the anisotropy of $\alpha^{(3)}$ and $\beta^{(3)}$ k^2 renormalization terms. We found that the qualitative agreement between the effective model and

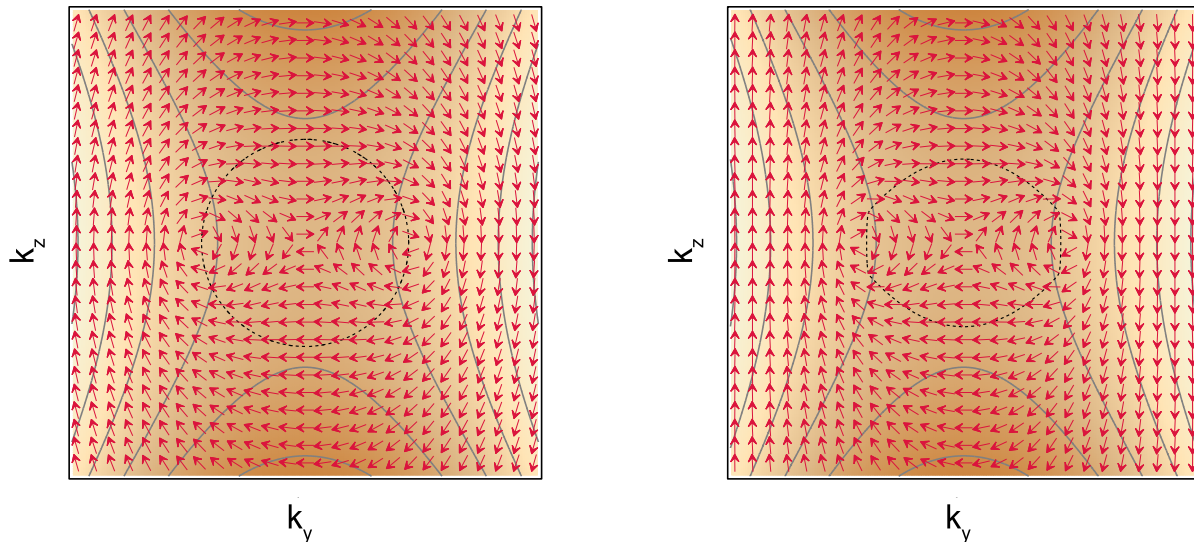


FIG. 6: Spin-polarization pattern evaluated from the $\mathbf{k} \cdot \mathbf{p}$ model Eq. (1) with different choices of the model parameters compatible with the results of the fitting procedure given in Table I. (Left panel) Spin texture for $\gamma_\alpha = \gamma_\beta = 0$ and $\alpha^{(3)} = 21.6 \text{ eV}\text{\AA}^3$, $\beta^{(3)} = -2.52 \text{ eV}\text{\AA}^3$. (Right panel) Spin texture for $\gamma/2 = \gamma_\alpha = -\gamma_\beta = -5.2 \text{ eV}\text{\AA}^3$, $\alpha^{(3)} = 26.8 \text{ eV}\text{\AA}^3$ and $\beta^{(3)} = 2.68 \text{ eV}\text{\AA}^3$, corresponding to an anisotropy factor $f = 0.1$. Since the $\mathbf{k} \cdot \mathbf{p}$ model is by construction accurate only around Γ , we plot the pattern in a small range around the Brillouin zone center. The dashed black loop around Γ highlights the k value where $\alpha(k)$ changes sign; the spin-polarization pattern inside (outside) the loop displays a Dresselhaus-like (Rashba-like) character.

the DFT results slightly improves for f between -0.1 and 0.1, as shown in Fig. 6(right panel), suggesting that an almost unidirectional spin-orbit field at large momenta might be further stabilized by a cubic Dresselhaus-like spin-momentum coupling³⁴.

TABLE I: Ab-initio values of the kinetic and spin-orbit parameters, evaluated from a fit close to the Γ point. The quantities $\frac{\hbar^2}{2m_y}$ and $\frac{\hbar^2}{2m_z}$ are in $\text{eV}\text{\AA}^2$. The units are $\text{eV}\text{\AA}$ and $\text{eV}\text{\AA}^3$, respectively, for the first and third order terms in k .

kinetic parameters		SOC parameters			
$\frac{\hbar^2}{2m_y}$	$\frac{\hbar^2}{2m_z}$	$\alpha^{(1)}$	$\beta^{(1)}$	$\alpha^{(3)} + \gamma_\alpha$	$\beta^{(3)} - \gamma_\beta$
15.9	8.59	-0.0102	-0.0145	21.6	-2.52

IV. CONCLUSIONS

In summary, we unveiled that the Dion-Jacobson layered perovskite $\text{CsBiNb}_2\text{O}_7$ possesses the unidirectional spin texture independent from the momentum over large areas of the Brillouin zone, which gives rise to the persistent spin helix and potentially long spin lifetimes. We emphasize that this peculiar spin wave mode emerges as an intrinsic property of the bulk phase, thus does not rely on fine tuning of Rashba and Dresselhaus parameters which was a strong requirement to realize the PSH in

semiconductor quantum wells explored in last years.^{34–39}

In particular, we have shown that the crystal symmetry (space group $P2_1am$) and the point group of the Γ point (C_{2v}) around which the spin-splitting occurs, perfectly match the requirements for the PSH design, as it allows for coexisting Rashba and Dresselhaus couplings. Our DFT calculations reveal that these SOC parameters compensate well and the spin texture can be considered quasi-independent from the momentum.

Finally, in contrast to similar ferroelectric oxides the spin-splitting is found in the valence band. Despite being rather small (10 meV) and related to higher-order spin-momentum coupling, it yields PSH which could be directly measured via ARPES, provided a sufficiently accurate resolution is reached. Moreover, as $\text{CsBiNb}_2\text{O}_7$ is a robust ferroelectric and an example of FERSC, a ferroelectric switching of PSH could be observed as well. We hope our results will be useful for realization of novel spintronics devices based on FERSC and will stimulate further search of similar materials with Rashba-Dresselhaus spin textures that could yield a persistent spin helix and, ideally, infinite spin lifetimes.

Acknowledgments

We thank Luiz Gustavo Davanese da Silveira and Sang-Wook Cheong for useful discussions. The work is supported by the Foundation for Polish Science through the IRA Programme co-financed by EU within SG OP. C.A. acknowledges the CINECA award under the ISCRA ini-

tiative IsC54 "CAMEO" and IsC69 "MAINTOP" Grant, for the availability of high performance computing re-

sources and support.

- ¹ S. Datta and B. Das, *Applied Physics Letters* **56**, 665 (1990).
- ² S. Picozzi, *Frontiers in Physics* **2**, 10 (2014).
- ³ D. Di Sante, P. Barone, R. Bertacco, and S. Picozzi, *Advanced Materials* **25**, 509 (2013).
- ⁴ M. Liebmann, C. Rinaldi, D. Di Sante, J. Kellner, C. Pauly, R. N. Wang, J. E. Boschker, A. Giussani, S. Bertoli, M. Cantoni, et al., *Advanced Materials* **28**, 560 (2016).
- ⁵ C. Rinaldi, S. Varotto, M. Asa, J. Sławińska, J. Fujii, G. Vinai, S. Cecchi, D. Di Sante, R. Calarco, I. Vobornik, et al., *Nano Letters* **18**, 2751 (2018).
- ⁶ J. Sławińska, D. Di Sante, S. Varotto, C. Rinaldi, R. Bertacco, and S. Picozzi, *Phys. Rev. B* **99**, 075306 (2019).
- ⁷ C. Rinaldi, J. C. Rojas-Sanchez, R. N. Wang, Y. Fu, S. Oyarzun, L. Vila, S. Bertoli, M. Asa, L. Baldrati, M. Cantoni, et al., *APL Materials* **4**, 032501 (2016).
- ⁸ E. Plekhanov, P. Barone, D. Di Sante, and S. Picozzi, *Phys. Rev. B* **90**, 161108 (2014).
- ⁹ A. Stroppa, D. Di Sante, P. Barone, M. Bokdam, G. Kresse, C. Franchini, M.-H. Whangbo, and S. Picozzi, *Nature Communications* **5**, 5900 (2014).
- ¹⁰ A. Narayan, *Phys. Rev. B* **92**, 220101 (2015).
- ¹¹ L. L. Tao, T. R. Paudel, A. A. Kovalev, and E. Y. Tsymlal, *Phys. Rev. B* **95**, 245141 (2017).
- ¹² L. G. D. da Silveira, P. Barone, and S. Picozzi, *Phys. Rev. B* **93**, 245159 (2016).
- ¹³ J. Varignon, J. Santamaria, and M. Bibes, *Phys. Rev. Lett.* **122**, 116401 (2019).
- ¹⁴ A. V. Kolobov, D. J. Kim, A. Giussani, P. Fons, J. Tom-inaga, R. Calarco, and A. Gruverman, *APL Materials* **2**, 066101 (2014).
- ¹⁵ H. Lee, J. Im, and H. Jin, *arxiv:1712.06112* (2018).
- ¹⁶ J. Schliemann, J. C. Egues, and D. Loss, *Phys. Rev. Lett.* **90**, 146801 (2003).
- ¹⁷ B. A. Bernevig, J. Orenstein, and S.-C. Zhang, *Phys. Rev. Lett.* **97**, 236601 (2006).
- ¹⁸ L. L. Tao and E. Y. Tsymlal, *Nature Communications* **9**, 2763 (2018).
- ¹⁹ H. Djani, A. C. Garcia-Castro, W.-Y. Tong, P. Barone, E. Bousquet, S. Picozzi, and P. Ghosez, *arXiv:1903.01241* (2019).
- ²⁰ G. Kresse and J. Furthmuller, *Computational Materials Science* **6**, 15 (1996).
- ²¹ G. Kresse and J. Furthmuller, *Phys. Rev. B* **54**, 11169 (1996).
- ²² P. E. Blöchl, *Phys. Rev. B* **50**, 17953 (1994).
- ²³ G. Kresse and D. Joubert, *Phys. Rev. B* **59**, 1758 (1999).
- ²⁴ J. P. Perdew, K. Burke, and M. Ernzerhof, *Phys. Rev. Lett.* **77**, 3865 (1996).
- ²⁵ A. Snedden, K. S. Knight, and P. Lightfoot, *Journal of Solid State Chemistry* **173**, 309 (2003).
- ²⁶ S. Roy, C. Autieri, B. Sanyal, and T. Banerjee, *Scientific Reports* **5**, 15747 (2015).
- ²⁷ C. Autieri, *Journal of Physics: Condensed Matter* **28**, 426004 (2016).
- ²⁸ D. Vanderbilt and R. D. King-Smith, *Phys. Rev. B* **48**, 4442 (1993).
- ²⁹ C. J. Fennie and K. M. Rabe, *Applied Physics Letters* **88**, 262902 (2006).
- ³⁰ N. A. Benedek, *Inorganic Chemistry* **53**, 3769 (2014).
- ³¹ H. Sim and B. G. Kim, *Phys. Rev. B* **89**, 144114 (2014).
- ³² C. Autieri, M. Cuoco, and C. Noce, *Phys. Rev. B* **85**, 075126 (2012).
- ³³ C. Autieri, M. Cuoco, and C. Noce, *Phys. Rev. B* **89**, 075102 (2014).
- ³⁴ M. Kohda, V. Lechner, Y. Kunihashi, T. Dollinger, P. Olbrich, C. Schönhuber, I. Caspers, V. V. Bel'kov, L. E. Golub, D. Weiss, et al., *Phys. Rev. B* **86**, 081306 (2012).
- ³⁵ J. D. Koralek, C. P. Weber, J. Orenstein, B. A. Bernevig, S.-C. Zhang, S. Mack, and D. D. Awschalom, *Nature* **458**, 610 EP (2009).
- ³⁶ M. P. Walser, C. Reichl, W. Wegscheider, and G. Salis, *Nature Physics* **8**, 757 EP (2012).
- ³⁷ J. Ishihara, Y. Ohno, and H. Ohno, *Applied Physics Express* **7**, 013001 (2013).
- ³⁸ F. Passmann, S. Anghel, T. Tischler, A. V. Poshakinskiy, S. A. Tarasenko, G. Karczewski, T. Wojtowicz, A. D. Bristow, and M. Betz, *Phys. Rev. B* **97**, 201413 (2018).
- ³⁹ P. Altmann, F. G. G. Hernandez, G. J. Ferreira, M. Kohda, C. Reichl, W. Wegscheider, and G. Salis, *Phys. Rev. Lett.* **116**, 196802 (2016).